sustainability

MDPI

Article

The Lithium-Ion Battery Temperature Field Prediction Model Based on CNN-Bi-LSTM-AM

Boyu Wang [1,2], Zheying Chen [1], Puhan Zhang [3], Yong Deng [3] and Bo Li [1,3,*]

[1] Nanchang Innovation Institute, Peking University, Nanchang 330000, China; 20220131@stu.cqu.edu.cn (B.W.)
[2] Cincinnati Joint Co-op Institute, Chongqing University, Chongqing 400044, China
[3] College of Engineering, Peking University, Beijing 100080, China
* Correspondence: bo.li@pku.edu.cn

Abstract: This study focuses on the internal temperature field of lithium-ion batteries, aiming to address the temperature variation issues arising from complex operating conditions in new energy batteries. To cope with unpredictable temperature fluctuations and long delay times, we propose an enhanced Convolutional Bidirectional Long Short-Term Memory Neural Network (CNN-Bi-LSTM-AM) model for temperature field prediction. The model integrates CNN for spatial feature extraction, Bi-LSTM for capturing temporal characteristics, and an attention mechanism to enhance the identification of key time-series features. By simulating temperature variations through a lumped model and thermal runaway model, we generate temperature field data, which are then utilized by the deep learning model to effectively capture the complex nonlinear relationships between temperature, voltage, state of charge (SOC), insulation resistance, current, and the internal temperature field. Performance evaluation using accuracy metrics and validation under various environmental conditions demonstrates that the model improves prediction accuracy by 1.2–2.3% compared to traditional methods (e.g., ARIMA, LSTM) with only a slight increase in testing time. Comprehensive evaluations, including ablation studies, thermal runaway tests, and computational efficiency analysis, further validate the robustness and applicability of the model. Furthermore, this study contributes to the optimization of battery life and safety by enhancing the prediction accuracy of the internal temperature field, thereby reducing resource waste caused by battery performance degradation. The findings provide an innovative approach to advancing new energy battery technology, promoting its development toward greater safety, stability, and environmental sustainability, which aligns with global sustainable development goals.

Keywords: lithium-ion battery; Convolutional Neural Network (CNN); Bidirectional LSTM (Bi-LSTM); temperature field prediction model; environmental impact

check for updates

Academic Editor: Osama Sohaib

Received: 30 December 2024
Revised: 14 February 2025
Accepted: 23 February 2025
Published: 1 March 2025

Citation: Wang, B.; Chen, Z.; Zhang, P.; Deng, Y.; Li, B. The Lithium-Ion Battery Temperature Field Prediction Model Based on CNN-Bi-LSTM-AM. *Sustainability* **2025**, *17*, 2125. https://doi.org/10.3390/su17052125

Copyright: © 2025 by the authors. Licensee MDPI, Basel, Switzerland. This article is an open access article distributed under the terms and conditions of the Creative Commons Attribution (CC BY) license (https://creativecommons.org/licenses/by/4.0/).

1. Introduction

In recent years, with the rapid development of the new energy industry, energy-efficient and low-power electric vehicles (EVs) have become a key focus for many countries, with lithium-ion batteries emerging as one of the core technologies for these vehicles [1,2]. However, lithium-ion batteries face several challenges during charge and discharge cycles, including an increasing number of cycles [3], significant fluctuations in charge and discharge currents [4], and reduced charge and discharge durations [5]. Additionally, overcharging can lead to charge overload, resulting in thermal runaway and increased temperature fluctuations, which pose a significant threat to battery safety [6]. Therefore, an efficient thermal management strategy has become a critical issue that needs to be

addressed. Under complex operating conditions, parameters such as electrochemical reactions, capacity, and internal resistance experience significant changes, leading to more pronounced nonlinear polarization phenomena [7,8], which, in turn, increase internal resistance and heat generation [9,10]. As heat accumulates, internal temperature fluctuations within the battery intensify [11]. If these temperature variations are not accurately predicted and controlled, they can lead to the failure of the thermal management system, endangering the battery's operational safety. Therefore, accurately predicting and controlling the temperature fluctuations of lithium-ion batteries has become a crucial challenge in enhancing battery performance, ensuring the safety of electric vehicles, and extending battery lifespan.

Currently, models for studying battery thermal behavior and predicting battery temperature are primarily categorized into two types: one based on internal chemical reactions, exploring the relationship between heat generation and heat transfer, and the other using neural networks for supervised learning to achieve effective temperature predictions. Chemical reaction-based methods include electrochemical–thermal coupling models [12], electrical–thermal coupling models [13], and thermal abuse models [14]. Kang, Hu, and others [15] conducted pulse charge experiments at different temperatures to calibrate solid-phase diffusion coefficients and reaction rate constants, developing an electrochemical–thermal couple model to predict the temperature of lithium-ion batteries. Zhang [16] improved temperature prediction accuracy by further coupling a heat generation model to the isothermal model. Kobayashi, Nakada, and others [17] employed finite element analysis (FEA) to construct a three-dimensional (3D) electrochemical–thermal coupling model, accurately simulating the temperature distribution and dynamic changes inside the lithium-ion battery. Han, Liu, and others [18] were the first to combine equivalent circuit models (ECM) with thermal models, indirectly estimating the battery's internal temperature by measuring voltage and current changes. However, these chemical reaction-based methods are slow to respond under complex operating conditions, making it difficult to monitor battery abnormalities in real-time. As a result, batteries may suffer thermal damage due to delayed thermal management, which does not meet the real-time monitoring and management needs of Battery Management Systems (BMSs).

In contrast, by optimizing the environment and duration for training and prediction, data-driven models can achieve higher computational efficiency. Using historical or real-time data, self-learning models can capture latent correlations to predict the temperature on the surface of lithium-ion batteries, thus avoiding the need for complex electrochemical process modeling. Zhang, Ma, and others [19] demonstrated that recurrent neural networks (RNNs) perform well in temperature field prediction for various types of batteries. Zhou, Liu, and others [20] proposed an innovative GRU-RNN model for predicting the temperature field of Nickel Manganese Cobalt (NMC) and Lithium Iron Phosphate (LFP) batteries, demonstrating strong performance with a relatively small number of hidden neurons. Li, Shen, and others [21] proposed a momentum-optimized GRU-RNN model, highlighting the significance of Long Short-Term Memory (LSTM) networks in capturing temporal dependencies while also demonstrating the advantages of Bi-LSTM and Bi-GRU models in capturing bidirectional temporal dependencies. Wang et al. [22] integrated Convolutional Neural Networks (CNN) with LSTM, achieving a significant improvement in the accuracy of temperature prediction. Research has shown that convolutional layers can effectively extract local features, while LSTMs can capture time-series information, enhancing the overall performance of the model. Additionally, literature [23] proposed a hybrid model combining LSTM and self-attention mechanisms, further enhancing the prediction capability for dynamic temperature field changes.

To improve the accuracy of the data-driven model, attention mechanisms have been introduced in the literature [24,25]. The attention mechanism dynamically adjusts the importance of different input features, focusing on key attributes. This approach enhances the model's learning efficiency and predictive accuracy when handling complex input sequences. In the field of temperature field prediction, Tian, Huang, and others [26] validated the effectiveness of the attention mechanism. Their research demonstrated that the Bi-LSTM model with the attention mechanism significantly outperforms the model without it in terms of prediction accuracy. This result highlights the ability of the attention mechanism to improve model performance and stability, especially in complex tasks like temperature field prediction.

This study presents an innovative approach for monitoring the internal temperature field of lithium-ion batteries. First, temperature field data are generated through electrochemical-thermal model simulations. Then, a data-driven model is trained using this data, and the proposed CNN-Bi-LSTM-AM model is employed for accurate temperature field prediction. The model is trained and tested under simulated environmental conditions, demonstrating outstanding performance. In the future, users will only need to input the relevant battery parameters to quickly obtain temperature field predictions for the next 30 s, enabling efficient real-time monitoring and management. The main contributions of this paper are summarized as follows:

1. This study represents the first attempt to generate the training data necessary for deep learning models via simulations of electrochemical reaction models. The authenticity and validity of the dataset are validated through terminal voltage calculations, offering a novel approach for large-scale training;
2. The proposed CNN-Bi-LSTM-AM model integrates convolutional layers with Bi-LSTM, leveraging the self-attention mechanism to selectively focus on key features, thereby improving the accuracy of temperature field predictions;
3. The model demonstrates exceptional generalization ability and overall performance through training and testing under various initial conditions;
4. This model provides the first validation of the effective application of deep learning in predicting battery thermal runaway scenarios.

The structure of the rest of the paper is as follows: Section 1 outlines the process of generating training data using the Lumped Model. Section 2 introduces the CNN-Bi-LSTM-AM model structure proposed in this study. Section 3 evaluates the effectiveness of the model through case studies. Section 4 concludes with final remarks. We hereby emphasize that all evaluations of related works presented in this section are original.

2. Datasets

In practical experiments, multiple temperature sensors are installed on lithium-ion battery cells, and thermal runaway conditions are induced through cyclic charging to obtain accurate thermal runaway temperature field data. However, the rapid rise in temperature during the thermal runaway process may cause equipment damage, leading to high experimental costs and time consumption. To reduce costs and improve efficiency, this study introduces, for the first time, the use of an electrochemical reaction model to simulate real-world data, generating temperature field data for training purposes. This section will first describe the electrochemical simulation process for the temperature field and then detail the filtering process applied to the generated data.

2.1. Lumped Model

This study initially employs a lumped model to simulate the normal temperature rise in the temperature field data of lithium-ion batteries. The lumped model simulates

three primary effects during the battery's operation: Ohmic effect, polarization effect, and concentration gradient effect, enabling real-time reflection of the battery's state. Additionally, the model's simplicity makes it suitable for rapid thermal analysis of large battery packs. The physical simulation model of the battery is illustrated in Figure 1. According to the Bernardi heat generation model, the heat generation rate inside the battery is defined as follows:

$$Q = \frac{I}{V_b}(U - V) + \frac{I}{V_b}(T\frac{dU}{dT}) = \frac{I}{V_b}((\eta_{ohm} + \eta_{act} + \eta_{conc}) + T\frac{dU}{dT}) \quad (1)$$

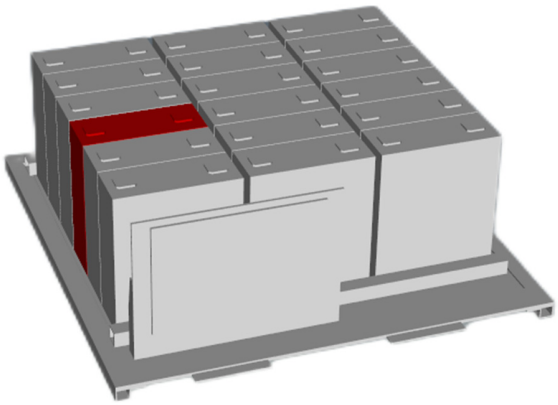

Figure 1. Schematic of the 3D grid for the 18-cell battery pack.

Here, I represents I_{app}, the applied current, V_b is the cell volume, and $\frac{dU}{dT}$ is the temperature derivative of the open-circuit voltage. U denotes the open-circuit voltage, V is the terminal voltage, η_{ohm} represents the Ohmic overpotential, η_{act} is the activation overpotential, and η_{conc} is the concentration overpotential. The lumped model focuses on solving these three overpotentials internally to analyze the thermal and electrochemical behavior of the battery.

The simulation process for the Ohmic overpotential is as follows:

$$\eta_{ohm} = I * R_{ohm} \quad (2)$$

$$R_{ohm} = R_{ref_ohm} * exp(\frac{E_{a_{ir}}}{R_{ref_ohm}}(\frac{1}{T} - \frac{1}{T_{ref}})) \quad (3)$$

Here, $E_{a_{ir}}$ represents the activation energy of the Ohmic resistance and R_{ref_ohm} denotes the Ohmic resistance of the battery.

The calculation method for the activation overpotential is derived by inverting the well-known Butler–Volmer (BV) equation. The simulation process is as follows:

$$\eta_{act} = \frac{2RT}{F} arcsinh(\frac{I}{2I_0}) \quad (4)$$

$$I_0 = I_{0,\,ref} * exp(\frac{E_{aJ_0}}{R}(\frac{1}{T} - \frac{1}{T_{ref}})) \quad (5)$$

Here, I_0 represents the activation current density, R and F are the ideal gas constant and Faraday's constant, respectively. I_0 denotes the exchange current density and E_{aJ_0} represents the activation energy of the activation overpotential.

The simulation process for the concentration overpotential is as follows:

$$\tau\frac{\mathrm{dS}}{\mathrm{dt}} + \nabla\cdot(-\nabla \mathrm{S}) = 0 \quad (6)$$

$$-\nabla S = 0 \quad x = 0 \quad -\nabla S = \frac{\tau I}{3Q} \quad x = 1 \tag{7}$$

The concentration overpotential models the battery as a sphere with a radius of 1. S represents the concentration distribution along the radial direction of the sphere, and Q denotes the battery capacity. τ represents the characteristic time, analogous to the diffusion coefficient in a diffusion equation.

Ekström et al. [27] fitted the parameters in the lumped model (including R_{ref_ohm}, $I_{0,\,ref}$, and τ) through the experimental data, and compared the mean square error between model prediction and the experimental data under 253.15 K and 298.15 K. It shows that this model performed well at room temperature with a standard deviation of around 10 mV and around 20 mV standard deviation under the cold environment. Therefore, the lumped model provides an effective tool for simulating and optimizing battery thermal management systems.

2.2. Thermal Runaway Model

Battery thermal runaway refers to a series of chain chemical reactions due to certain causes, which generate a large amount of heat, leading to a rapid rise in temperature that becomes uncontrollable. Recently, the mathematical model has been formulated using the Arrhenius equations for the different reactions, including SEI (Solid Electrolyte Interface) decomposition, negative-solvent reaction, positive-solvent reaction, and electrolyte decomposition reaction [28]. The mathematical formula is as follows:

$$\frac{dc_{sei}}{dt} = -A_{sei} exp\left[-\frac{E_{sei}}{RT}\right] c_{sei} \tag{8}$$

$$\frac{dc_{ne}}{dt} = -A_{ne} exp\left(-\frac{t_{sei}}{t_{\text{sei }ref}}\right) exp\left[-\frac{E_{ne}}{RT}\right] c_{ne} \tag{9}$$

$$\frac{d\alpha}{dt} = A_{pe} exp\left[-\frac{E_{pe}}{RT}\right] \alpha(1-\alpha) \tag{10}$$

$$\frac{dc_e}{dt} = -A_e exp\left[-\frac{E_e}{RT}\right] c_e \tag{11}$$

$$\dot{q}_{abuse} = H_{sei} W_{sei} \left|\frac{dc_{sei}}{dt}\right| + H_{ne} W_{ne} \left|\frac{dc_{ne}}{dt}\right| + H_{pe} W_{pe} \left|\frac{d\alpha}{dt}\right| + H_e W_e \left|\frac{dc_e}{dt}\right| \tag{12}$$

The explanations of the relevant parameters are listed in Table 1, along with the values of these parameters used in the experiments of this study.

Table 1. The explanation list.

Variable	Description	Unit	Value
c_{sei}	dimensionless amount of lithium-containing meta-stable species in the SEI	1	0.15
c_e	dimensionless concentration of electrolyte	1	1
α	degree of conversion	1	0.04
c_{ne}	dimensionless amount of lithium intercalated within the carbon	1	0.75
E_{se}	SEI-decomposition activation energy	J/mol	135,080
E_{ne}	Negative-solvent activation energy	J/mol	135,080
E_{pe}	Positive-solvent activation energy	J/mol	139,600
E_e	Electrolyte decomposition activation energy	J/mol	274,000
A_{se}	SEI-decomposition frequency factor	s^{-1}	1.667×10^{15}
A_{ne}	Negative-solvent frequency factor	s^{-1}	2.5×10^{13}
A_p	Positive-solvent frequency factor	s^{-1}	6.667×10^{13}

Table 1. *Cont.*

Variable	Description	Unit	Value
A_e	Electrolyte decomposition frequency factor	s^{-1}	5.14×10^{25}
W_{sei}	Specific negative content in jellyroll	g/m^3	6.104×10^5
W_{ne}	Specific negative content in jellyroll	g/m^3	6.104×10^5
W_{pe}	Specific positive active content in jellyroll	g/m^3	1.221×10^6
W_e	Specific electrolyte content in jellyroll	g/m^3	4.069×10^5
H_{sei}	SEI-decomposition heat release	J/g	257
H_{ne}	Positive-solvent heat release	J/g	1714
H_{pe}	Positive-solvent heat release	J/g	314
H_e	Electrolyte decomposition heat release	J/g	155

Figure 2 illustrates the temperature and sequence at which each reaction occurs. Thermal runaway is a typical chain reaction process that often occurs in batteries or other chemical systems. In this process, the decomposition of the solid electrolyte interphase (SEI) serves as the initial trigger, releasing a significant amount of heat that initiates subsequent chemical reactions. As heat continues to be generated, the reaction rates accelerate, with each reaction reinforcing the others, creating a self-amplifying positive feedback loop. This loop causes the reactions to persist and the heat accumulation to grow exponentially, ultimately leading to temperature runaway and, consequently, thermal runaway. Each reaction in the diagram corresponds to Equations (8)–(11), illustrating the chemical kinetics and temperature dependence of each reaction stage.

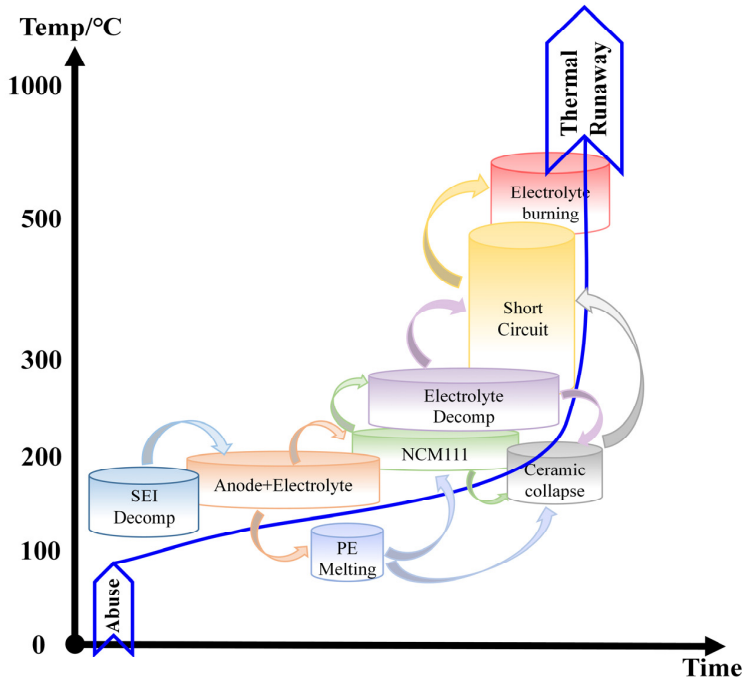

Figure 2. The temperature at which each reaction occurs and their respective sequence.

These reactions typically occur at higher temperatures; therefore, many thermal runaway reactions are often triggered by internal short circuits, which convert electrical energy into heat.

Here, we use a device [29] that can trigger the internal short circuit once the battery reaches a certain temperature. The formula is as follows:

$$\frac{dSoC}{dt} = -ISC_{cond} \cdot SoC \cdot A_{ec} \cdot exp\left(-\frac{E_{ec}}{RT}\right) \quad (13)$$

$$ISC_{\text{cond}} = \begin{cases} 0 \text{ for } T < 57\ ^{\circ}C \\ 1 \text{ for } T \geq 57\ ^{\circ}C \end{cases} \tag{14}$$

$$\dot{Q}_{ec} = -h_{ec}\frac{dSoC}{dt} \tag{15}$$

A_{ec} is the frequency factor. h_{ec} represents the electric energy that can be converted to heat energy, SoC is the state of charge. E_{ec} is the activation energy.

2.3. Dataset Description

In this research, the modeled lithium-ion battery pack compromises 18 series-connected prismatic cells. Each cell has 228 Ah nominal capacity and 2.04×10^{-3} m^3 volume.

The datasets applied in our model contain 325 samples acquired by thermal simulation. Through the finite element method, 7806 nodes are constructed on a battery pack. The simulation time for each sample is 1800 s with 120 time steps, while each time step takes 15 s. At the initial time, all cells in the battery pack have 0 SOC. And their initial temperature is 20 °C, the same as the ambient temperature.

There are 25 kinds of charging current curves (as shown in Figure 3a): 3 constant current curves, 8 linear current curves, 3 quadratic current curves, and 11 combined curves. Charge rates range from 1 C to 4 C. The diverse current curves enable neural networks to have strong generalization ability for different current forms.

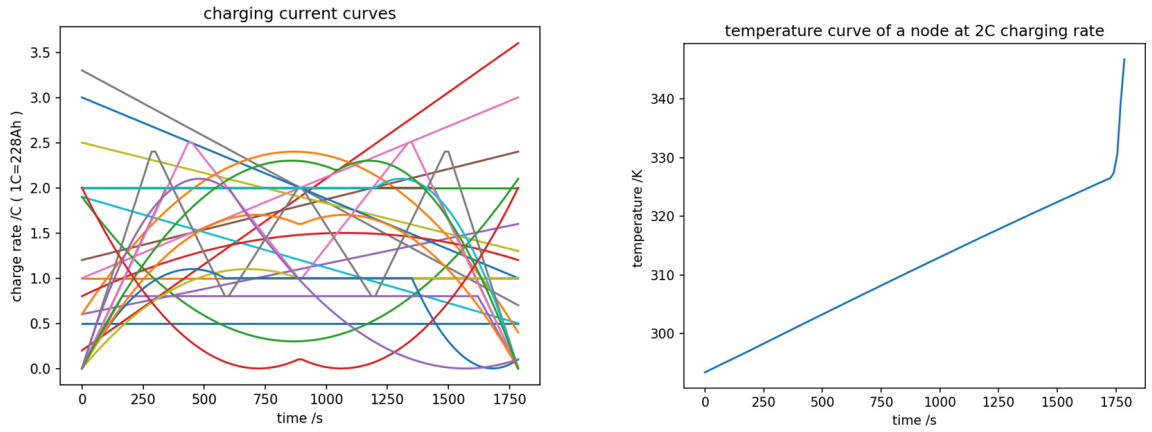

(**a**) (**b**)

Figure 3. (**a**) Twenty-five kinds of charging current curves; (**b**) temperature curve of a node at 2 C charging rate (456 A).

The ambient temperature is fixed at 20 °C. The cooling liquid that flows under the battery pack has 13 kinds of temperatures, ranging from 293.15 K to 313.15 K. And the temperature of the cooling liquid is linearly changed from inlet to outlet. The diverse temperature distributions enable neural networks to adapt to different temperature environments.

As a result, with a different combination of 25 current curves and 13 cooling liquid temperatures mentioned above (as illustrated in Figure 3a), we obtained the datasets of 325 battery conditions. And in each condition, we simulated the temperature variation of 7806 nodes in 1800 s.

Figure 3b illustrates the simulation result that a node's temperature changes when at 2 C constant charging rate (456 A). This node is on the battery cell, starting from the initial temperature of 293.15 K. As the charging process goes on, the temperature keeps increasing. When the temperature reaches 330 K, thermal runaway happens, resulting in a rapid temperature surge.

The input and output of the neural network are discrete values. The input consists of a sliding window of 120 consecutive data points, including current, voltage, ambient temperature, state of charge (SOC), and battery load. The output is the temperature at the next time step following the current time step. By training the neural network on these input data, we aim to enable it to identify changes in relevant parameters and predict abnormal temperature rises in the battery's thermal field in advance. We anticipate that this predictive capability will provide valuable support for early warning systems, particularly for potential issues such as thermal runaway.

2.4. Data Filtering

In order to achieve accurate model establishment and validation, we performed preprocessing on the data, including zero-padding, outlier correction, and other operations. The rules are as follows.

(1) Null Value Filling: If D_t is null, let

$$D_t = D_{t-1}$$

where D_t is the parameter at time step t.

(2) Outlier Correcting: If P_t is out of normal range, let

$$P_t = P_{t-1}$$

The normal ranges of temperature, battery voltage, SOC, insulation resistance, and battery current are $(-40\ ^\circ\text{C}, +\infty)$, (2 V, 5 V), (0, 100%), $(0, +\infty)$, and (−1400 A, 1400 A), respectively.

(3) Data Filtering: Data preprocessing can be integrated with deep learning to enhance its applicability in real-world scenarios, as shown in Figure 4. When new time step data D_t is generated, historical data are extracted using a sliding window and sequentially processed through null value filling, outlier correction, and filtering. The processed data are then fed into the neural network for rolling prediction of subsequent time steps.

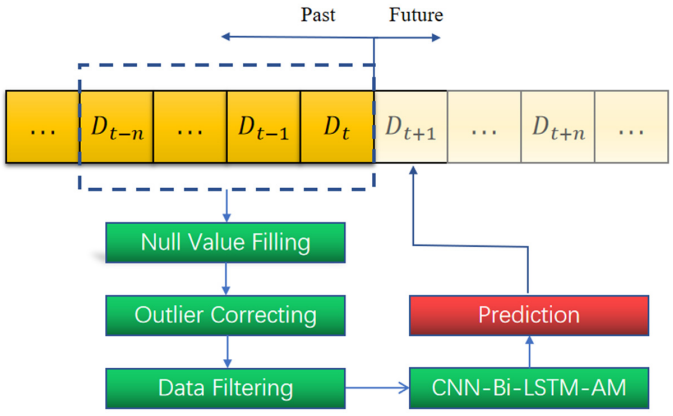

Figure 4. Data preprocessing procedure.

3. Methods

Bi-LSTM networks are proficient in autonomously learning complex nonlinear temporal patterns hidden in the data, while CNNs specialize in integrating information across different dimensions. In this study, we propose a CNN-Bi-LSTM model based on the self-attention mechanism, which combines the strengths of CNN and Bi-LSTM to predict the temperature field of lithium-ion batteries. Figure 5 illustrates the flowchart of the CNN-Bi-LSTM-AM model.

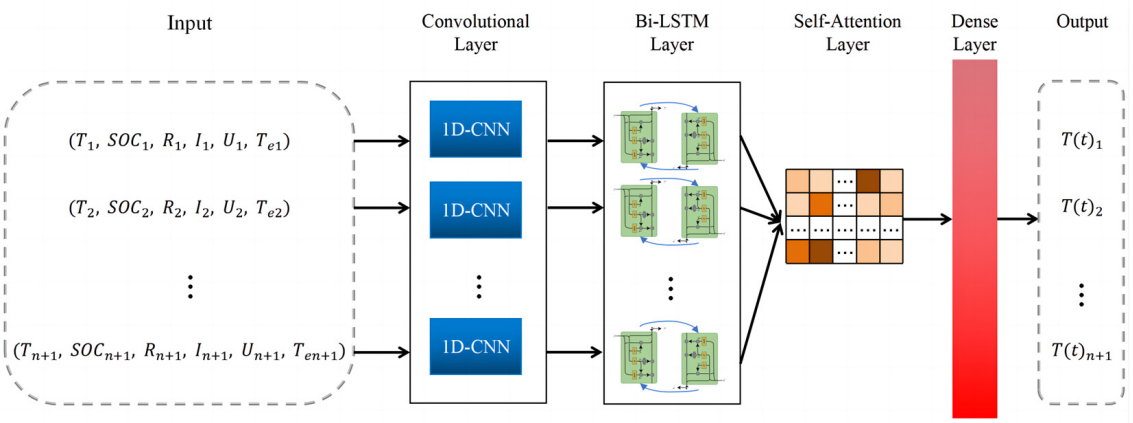

Figure 5. Architecture diagram of a CNN-Bi-LSTM self-attention Network for time-series data prediction.

3.1. CNN and Bi-LSTM

Convolutional Neural Network (CNN), a variant of feedforward neural networks, was proposed by Lecun et al. [30]. CNN extracts spatial features from raw data by focusing on local information. Its main structure comprises an input layer, convolutional layers, pooling layers, fully connected layers, and an output layer. The convolutional layer contains a set of convolutional filters used to extract spatial features of the input data. Different filters (or convolutional kernels) are applied to data processing in the convolutional layer to generate feature maps, thereby helping the neural network to perform regression or classification on input data more effectively.

In practical applications, the Two-Dimensional Convolutional Neural Network (2D-CNN) is widely used in computer vision and image processing to extract features from input images, while the One-Dimensional Convolutional Neural Network (1D-CNN) is mainly used for signal processing to extract features from time-series data. In this study, the 1D-CNN receives five measurable battery signals: current, voltage, ambient temperature, SOC, battery load, etc., in order to express the interrelationships among the input parameters.

The Bidirectional Long Short-Term Memory (Bi-LSTM) model is an extension of the LSTM model [31], and its internal structure is shown in Figure 6. The Bi-LSTM model consists of two main parts: one LSTM model for the forward processing of past input features and another LSTM model for the backward processing of future input features. This characteristic of Bi-LSTM enables it to perform excellently in the prediction task of long sequence data and significantly improves the prediction accuracy.

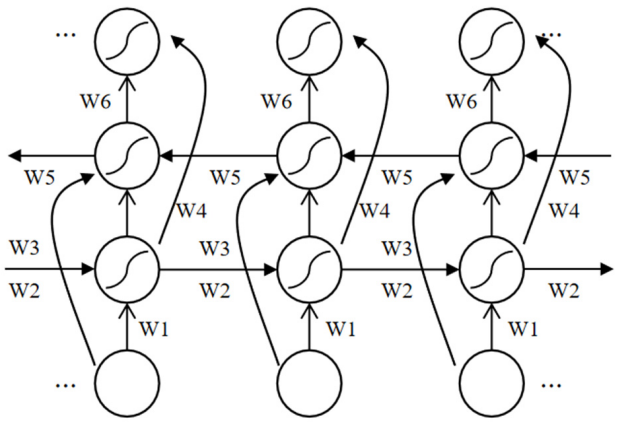

Figure 6. Bi-LSTM neuron structure.

To solve the gradient vanishing and exploding problem, the Bi-LSTM network combines three gates: the input gate (i_t), the forget gate (f_t), and the output gate (o_t). For the input sequence $\langle x_1, x_2, \ldots x_T \rangle$, the key equations are as follows:

$$\begin{aligned} f_t &= \sigma_g\Big(W_f x_t + U_f h_{t-1} + b_f\Big), \\ i_t &= \sigma_g(W_i x_t + U_i h_{t-1} + b_i), \\ o_t &= \sigma_g(W_o x_t + U_o h_{t-1} + b_o), \\ c_t &= f_t \circ c_{t-1} + i_t \circ \sigma_c(W_c x_t + U_c h_{t-1} + b_c), \\ h_i &= o_t \circ \sigma_h(c_t), \end{aligned} \tag{16}$$

Among them, the symbol $\circ$ represents the Hadamard product, x_t is the input of the unit at time t ; h_t is the output at the corresponding time step; c_t is the memory unit of the hidden unit; i_t, f_t, and o_t are the activation vectors of the input gate, forget gate, and output gate, respectively. The parameters W, U, and B are the weight matrices and bias parameters that need to be learned during the training process, σ_g is the sigmoid activation function, σ_c and σ_h is the hyperbolic tangent function. In the Bi-LSTM network, the final output hidden state h_t is generated by concatenating the forward hidden state $h_t^{\rightarrow}$ and the backward hidden state $h_t^{\leftarrow}$.

3.2. Self-Attention Mechanism

The Attention Mechanism is a deep learning technique used to dynamically adjust the degree of attention that a model pays to input features. In the attention mechanism, the model consists of an encoder network and a decoder network, which map the input sequence to the desired target. The encoder network compresses the information of the input sequence into a context vector and passes its final state to the first unit of the decoder network.

The Self-attention Mechanism is a specific type of attention mechanism that enables the model to selectively focus on different parts of the input sequence when estimating the interdependencies among input elements. In this study, the Keras-self-attention library [32] is used to implement the self-attention mechanism. The self-attention is combined with the Bi-LSTM network to effectively capture the output sequence of the Bi-LSTM and train the independent layer through weight allocation, making it pay more attention to the most important output elements.

The main mathematical formula for the self-attention mechanism used to process sequence data and consider the context at each time step is as follows:

$$\begin{aligned} h_{t,t'} &= tanh\Big(W_g h_t + W_g'^{h_{t'}} + b_h\Big), \\ e_{t,t'} &= \sigma\big(W_e h_{t,t'} + b_e\big), \\ a_{t,t'} &= softmax\big(e_{t,t'}\big), \\ l_t &= \sum_{t'} a_{t,t'} h_{t'}, \end{aligned} \tag{17}$$

Among them, $h_{t,t'}$ is the output of the hidden node in the Bi-LSTM layer, $e_{t,t'}$ is the sigmoid activation output of the attention network, σ is the element-wise sigmoid function, and a_t is the softmax activation value. W_g and W_g' are the weight matrices corresponding to the hidden state h_t and $h_{t'}$ respectively, and W_e is the weight matrix of the attention network. Finally, l_t represents the attention-focused hidden state at a specific time step t, which is used to indicate the attention or importance that should be given to different neighboring elements (such as words or other input elements) [33]. Therefore, l_t captures the information related to the element corresponding to the current time step t,

and it is generated by performing attention calculations on the hidden states in the input sequence $h_{t'}$. The attention-focused hidden state representation l_t helps the model utilize contextual information, enhancing the understanding and representation of the input data. To calculate this attention-focused hidden state l_t, the model usually combines information based on the correlation of all time steps t' in the input sequence to highlight the associated information t of the current element at the time step.

3.3. CNN-Bi-LSTM-AM Model

By integrating CNN layers with Bi-LSTM units, the proposed network effectively captures both local spatial features and temporal dependencies from the input time series. Furthermore, a self-attention mechanism is incorporated to enhance the extraction of critical feature information and optimize the learning of attention weights. The network begins with an input layer that processes a sequence of battery features, including current, voltage, ambient temperature, SOC, and battery load. Subsequently, CNN extracts spatial characteristics from the raw data, while Bi-LSTM models temporal relationships by capturing both past and future dependencies at each time step. The self-attention layer, connected to the outputs of the Bi-LSTM units, further refines the extracted features by focusing on the most relevant information for prediction. Figure 7 presents the architecture and workflow of the CNN-Bi-LSTM-AM temperature field prediction model, along with its potential applicability in future use cases.

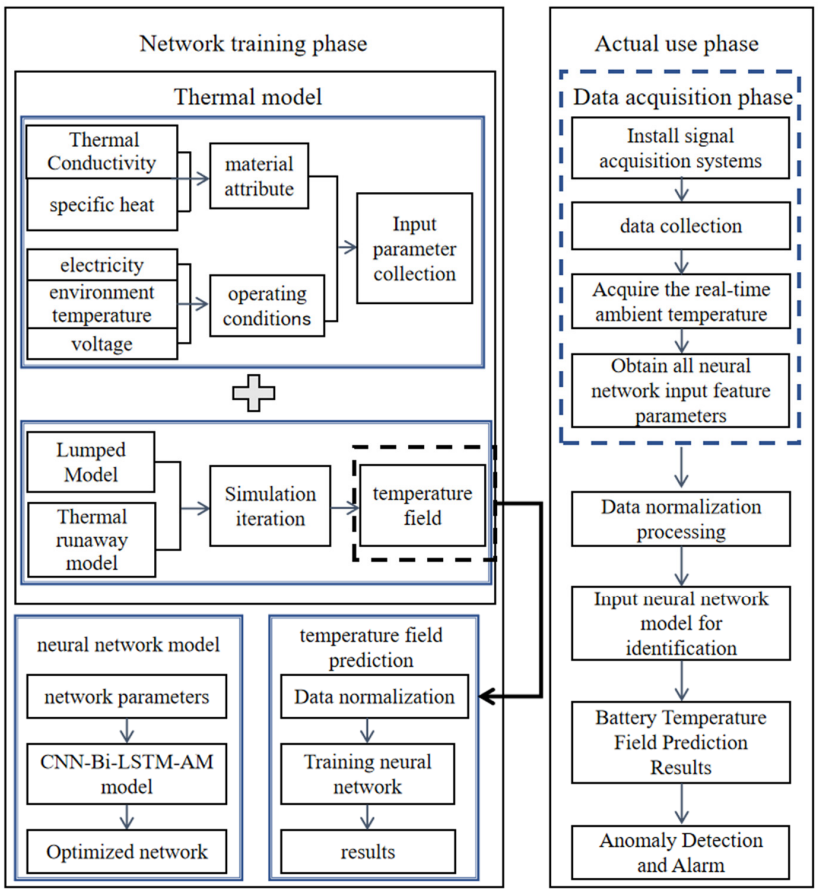

Figure 7. Prediction algorithm flow of the battery temperature field.

4. Results and Analysis

In this section, a comprehensive evaluation of the proposed CNN-Bi-LSTM-AM model was carried out. Its performance was compared with six deep learning models, namely, the

single LSTM, Bidirectional LSTM (Bi-LSTM), CNN-LSTM, CNN-Bi-LSTM, LSTM-AM, and the newly proposed CNN-Bi-LSTM-AM in this paper. To ensure the validity and scientific nature of the comparison, three evaluation metrics were selected, including the Root Mean Square Error (RMSE), Mean Absolute Error (MAE), and training time. At the same time, we will also deeply explore the impact of temperature factors on the models and the practical effects of each model in thermal runaway prediction so as to comprehensively and in-depth understand the characteristics, advantages, and disadvantages of different models.

4.1. Evaluation Metrics

To more effectively validate the effectiveness of the proposed scheme, we calculate the average Mean Absolute Error ($\overline{MAE}$) and Root Mean Square Error ($\overline{RMSE}$) across all nodes' temperature field predictions, and these averages are used as evaluation metrics for overall prediction performance. The specific expressions for MAE and RMSE are presented as follows:

$$\overline{MAE} = \frac{1}{K}\sum_{k=1}^{K}\left|y_{k,t} - \hat{y_{k,t}}\right| \tag{18}$$

$$\overline{RMSE} = \sqrt{\frac{1}{K}\sum_{k=1}^{K}\left(y_{k,t} - \hat{y_{k,t}}\right)^2} \tag{19}$$

Among them, K represents the total number of temperature field predictions, $y_{k,t}$ is the actual temperature field value of node k at time t, and $\hat{y_{k,t}}$ is the predicted temperature field value of node k at time t.

4.2. Experimental Environment

The experiment was conducted on the Windows 10 operating system. The neural network training of the simulated UCI datasets was carried out using the TensorFlow framework of Python 3.10. NVIDIA CUDA 11.2 was employed for GPU acceleration. The hardware components of this experiment consisted of an RTX 3070 Ti GPU, an i5-13400F 4.3 GHz CPU, and 16 GB of memory, as shown in Table 2.

Table 2. Experimental environment.

Hardware Environment	Software Environment
CPU: i5-13400F 4.3 GHz	Programming language: Python
Memory card: 16 GB	Programming platform: TensorFlow 2.6.0
Graphics card: NVIDIA CUDA 11.2	Operating system: Windows10

In the identical development environment, we divided 132 cases with different initial conditions into training and testing datasets in a 4:1 ratio and performed five-fold cross-validation. Each experiment was repeated 10 times. To guarantee the training effectiveness, during the training process, the network parameters were initialized as follows: Adam was selected as the optimizer, the learning rate was set to 0.0001, the batch size was fixed at 512, and the number of training epochs was 500.

The network architecture is illustrated in Figure 4. Specifically, the input data are first processed through a one-dimensional (1D) convolutional layer for feature extraction, with 64 filters of size 3, a stride of 1, and ReLU activation. This is followed by a bidirectional LSTM layer to capture temporal dependencies, with 60 LSTM units and a dropout rate of 0.5 to mitigate overfitting. To further enhance the model's focus on important features, an attention mechanism is incorporated, with 64 units in the attention layer. Finally, a fully connected layer is used to output the predicted temperature field for the next time step.

4.3. Baselines

To evaluate the proposed solution in this paper, we compare it against several baseline methods, ranging from simple benchmarks to state-of-the-art algorithms. The methods considered are as follows:

1. ARIMA (AutoRegressive Integrated Moving Average): ARIMA is a classical time series analysis method that models data using autoregression, differencing, and moving averages. It is well-suited for stationary or periodic time series data and offers simplicity with strong performance for univariate forecasting;
2. SVR (Support Vector Regression): SVR is a regression algorithm based on Support Vector Machines (SVM) and is effective for capturing nonlinear relationships. It maps input data to a higher-dimensional space using kernel functions and finds an optimal regression hyperplane;
3. LSTM (Long Short-Term Memory): LSTM is a variant of Recurrent Neural Networks (RNN) designed to address the gradient vanishing and explosion issues in long-term sequence modeling. By incorporating gating mechanisms, LSTM excels at capturing temporal dependencies in time series data;
4. CNN (Convolutional Neural Network): CNN extracts local spatial features through convolution and pooling operations, making it highly effective for spatial data analysis. For lithium-ion battery temperature field prediction, CNN can efficiently capture spatial temperature distribution patterns, particularly for two-dimensional or three-dimensional datasets.

4.4. Experimental Results

4.4.1. Comparison of Algorithms with Different Temperature Environments

Except for ARIMA, whose RMSE and MSE remain stable as the temperature increases, all other methods exhibit a trend of rising RMSE and MSE with higher initial environmental temperatures (as shown in Figure 8). In the dataset, when the ambient temperature ranges from 243.15 K to 293.15 K, our method significantly outperforms other approaches, particularly under low to moderate temperatures, demonstrating superior inference capability and robustness. This advantage highlights the model's adaptability and reliability in handling tasks within the low-to-moderate temperature range. However, when the temperature exceeds 293.15 K, the model may degrade into a standard LSTM, resulting in reduced feature extraction capability under high-temperature conditions. Under such circumstances, performance differences among methods become less pronounced, making it difficult to identify clear advantages. Overall, the experimental results underscore the robustness and inference strength of our approach in low-to-moderate temperature environments. Nevertheless, further optimization is required to maintain competitive performance in high-temperature scenarios. In Figure 9, we aim to present some typical temperature rise curves, and therefore, we have selected the temperature field prediction model for the normal charging of Cell 6 at 260 K.

4.4.2. Ablation Experiment

Table 3 investigates the specific impact of various modules on estimation metrics by systematically adding or removing components from the model. To evaluate the effectiveness of each module, we conducted a series of ablation experiments on the key modules illustrated in Figure 5. RMSE and MSE were used as evaluation metrics to comprehensively analyze the changes in model performance. In the experiments, we successively removed critical components such as CNN, Bi-LSTM, and the Attention Mechanism (AM) from the model. Additionally, we conducted substitution experiments by replacing Bi-LSTM with

LSTM to analyze the architectural differences further. The results of the experiments are shown in Table 3 below.

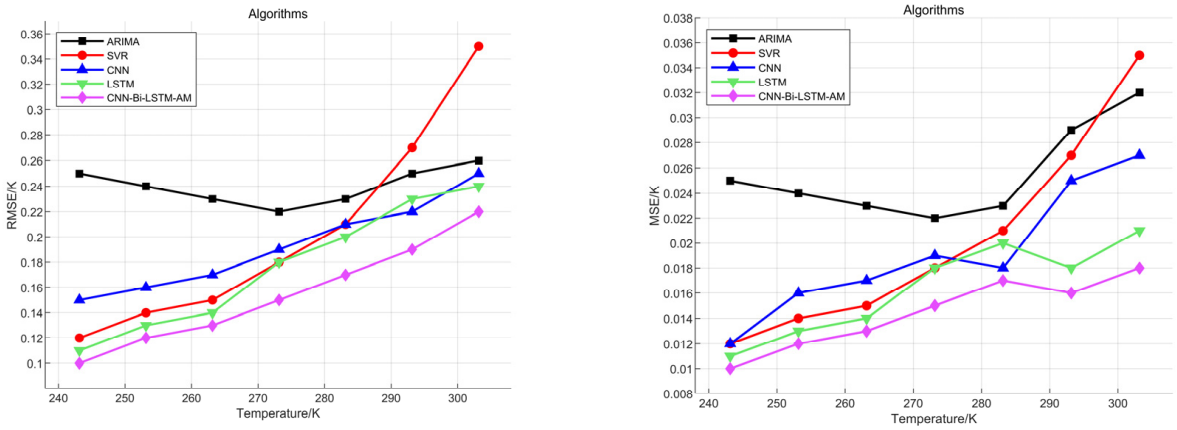

Figure 8. Error analysis results for each algorithm: (**a**) RMSE; (**b**) MSE.

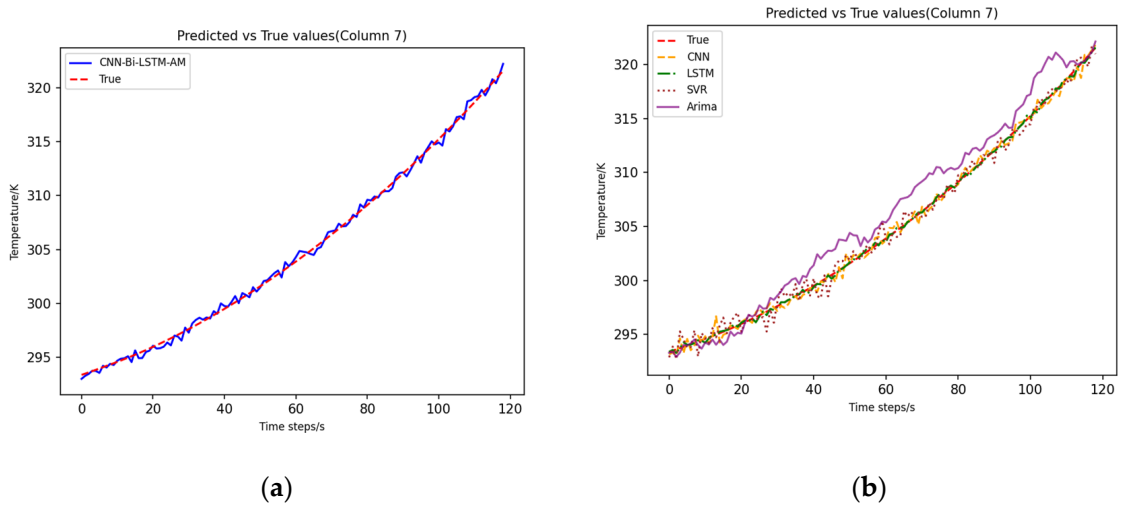

Figure 9. Temperature field prediction model for normal charging (Cell 6 of the battery cell, 260 K). (**a**) CNN-Bi-LSTM-AM; (**b**) baseline model.

Table 3. The computational performance (mean ± Std).

Algorithms	RMSE	MSE
CNN-Bi-LSTM-AM	0.0856 ± 0.0012	0.0073 ± 0.0004
CNN-Bi-LSTM	0.0912 ± 0.0015	0.0083 ± 0.0005
Bi-LSTM-AM	0.0895 ± 0.0014	0.0078 ± 0.0005
CNN-AM	0.0958 ± 0.0017	0.0092 ± 0.0006
CNN-LSTM-AM	0.0883 ± 0.0013	0.0076 ± 0.0005
CNN-LSTM	0.0930 ± 0.0016	0.0087 ± 0.0005
LSTM-AM	0.0902 ± 0.0015	0.0081 ± 0.0004

The simulation results, as shown in Table 2, compare the performance of LSTM and bidirectional Bi-LSTM networks with 60 hidden neurons under identical conditions for temperature field prediction. The results indicate that the Bi-LSTM model outperforms the LSTM model, achieving lower errors in both RMSE and MSE metrics. This suggests that temperature field variations depend not only on historical states but also on future informa-

tion. Compared to the unidirectional LSTM network, the Bi-LSTM network demonstrates superior capability in capturing global features of the temperature field, enabling more accurate modeling of spatiotemporal dependencies and exhibiting greater adaptability and predictive performance.

The combination of CNN and LSTM networks effectively captures the nonlinear dynamics of battery systems while extracting spatial and temporal features from the input data. In the subsequent analysis, we compared the performance of CNN-Bi-LSTM-AM, Bi-LSTM-AM, CNN-LSTM-AM, and LSTM-AM networks.

First, we compared the performance of a single-layer LSTM and a bidirectional Bi-LSTM network, both with 60 hidden neurons, under identical conditions for temperature field prediction. The results indicate that the CNN-Bi-LSTM network achieved an RMSE of 0.0912 and an MAE of 0.0083, significantly outperforming the CNN-LSTM network, which yielded an RMSE of 0.093 and an MAE of 0.0087. This suggests that temperature field variations are not only dependent on past states but also on future information. Therefore, in contrast to the unidirectional LSTM network, the Bi-LSTM network excels in capturing the global features of the temperature field, offering superior adaptability and predictive performance.

In addition, The experimental results demonstrate that incorporating CNN into the network architecture significantly outperforms using RNN-based networks alone. Specifically, the CNN-Bi-LSTM-AM network achieved reductions of 2.39% and 1.47% in RMSE and MAE, respectively, compared to the Bi-LSTM-AM network. Similarly, the CNN-LSTM-AM network reduced RMSE and MAE by 2.22% and 1.27%, respectively, compared to the LSTM-AM network. These results demonstrate that CNN significantly enhances the model's ability to extract spatial features, improving prediction accuracy, particularly in capturing the spatial distribution and variation patterns of the temperature field.

Finally, we analyzed the impact of the attention mechanism on model performance by comparing the hybrid models CNN-Bi-LSTM-AM, CNN-Bi-LSTM, CNN-LSTM-AM, and CNN-LSTM. The experimental results demonstrate that hybrid networks with an attention mechanism outperform those without it. Specifically, the CNN-Bi-LSTM-AM model with self-attention achieved reductions of 0.98% in RMSE and 0.78% in MAE compared to the CNN-Bi-LSTM model. Similarly, the CNN-LSTM-AM model reduced RMSE and MAE by 0.51% and 0.21%, respectively, compared to the CNN-LSTM model. These results indicate that while the self-attention mechanism brings only marginal improvements, its contributions to reducing RMSE and MAE are significant.

In practical applications, even slight reductions in RMSE and MAE can have substantial value, emphasizing the importance of designing models to enhance performance. For instance, in the field of electric vehicles, more accurate battery temperature field predictions can significantly improve battery safety and performance management. Precise temperature field predictions enable the Battery Management System (BMS) to monitor and regulate battery temperatures in real time, preventing overheating or overcooling, thereby reducing the risk of thermal runaway, extending battery lifespan, and ensuring vehicle stability.

4.4.3. Thermal Runaway Experiment

This study focuses on a specific thermal runaway heating scenario occurring during the eighth charging cycle and employs a rolling sliding time window approach to predict the temperature rise process in the test dataset. Table 4 compares the average RMSE and MSE performance of different models for thermal runaway prediction across the entire battery pack, while Figure 10 illustrates the detailed prediction results of the proposed method during the thermal runaway heating phase, with only the central point of the

cell selected for analysis and visualization. The experimental results demonstrate that the proposed model exhibits exceptional predictive performance during the thermal runaway heating phase, validating its reliability and applicability.

Table 4. The computational performance (mean ± Std).

Algorithms	RMSE	MSE
ARIMA	0.1023 ± 0.0014	0.0105 ± 0.0005
SVR	0.0954 ± 0.0012	0.0091 ± 0.0004
LSTM	0.0922 ± 0.0013	0.0088 ± 0.0004
CNN	0.0908 ± 0.0015	0.0082 ± 0.0005
CNN-Bi-LSTM-AM	0.0856 ± 0.0012	0.0073 ± 0.0004

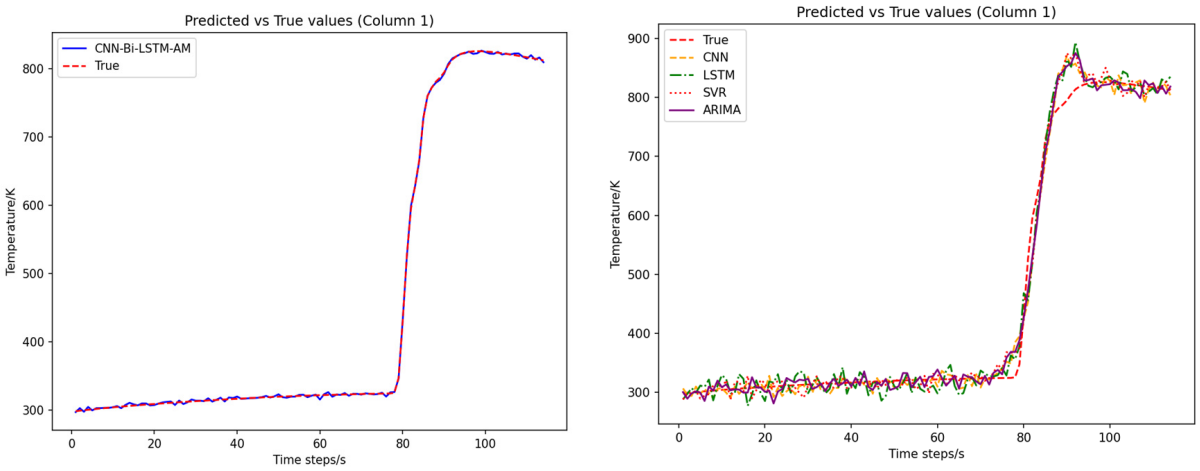

(**a**) (**b**)

Figure 10. Temperature field prediction model for thermal runaway heating (central node). (**a**) CNN-Bi-LSTM-AM; (**b**) baselines.

The experimental results demonstrate that the proposed model exhibits exceptional performance in thermal runaway prediction. Specifically, the CNN-Bi-LSTM-AM network outperforms the ARIMA, SVR, LSTM, and CNN models in terms of both RMSE and MAE. Among them, the ARIMA model performs the worst, with the highest RMSE and MAE values; the performance of SVR, LSTM, and CNN progressively improves, with CNN's prediction accuracy surpassing LSTM, closely approaching that of our CNN-Bi-LSTM-AM model. Notably, relying solely on time-series models struggles to accurately predict both the gradual temperature rise phase (i.e., the phase where the temperature increase slows) and the rapid heating phase (i.e., the phase of sharp temperature rise). However, models incorporating CNN and attention mechanisms are more effective and accurate in predicting the onset of thermal runaway. Therefore, we believe that the convolutional layers and attention mechanisms play a decisive role in capturing the timing of thermal runaway temperature increases. This finding is significant, as it provides new perspectives and directions for future research.

4.4.4. Computational Cost Efficiency

We conducted a fair comparison between our model, ARIMA, and other baseline methods. Each model was evaluated using five-fold cross-validation, with results averaged over 10 experiments. As shown in Figure 11, while our model required slightly more training time, the testing time across all models remained nearly identical. Importantly, our model achieved a significant improvement in prediction accuracy. In real-world

applications, testing performance is often more critical. Therefore, our model delivers substantial gains in accuracy at the cost of a modest increase in training time, enhancing its practical value.

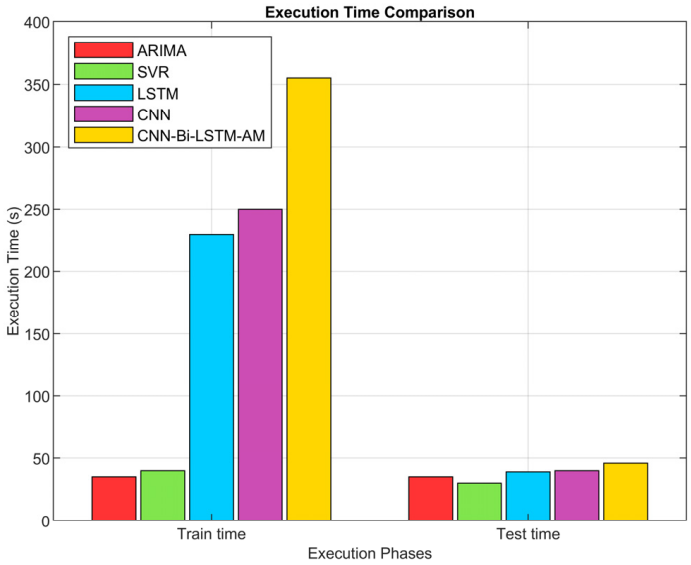

Figure 11. Execution time of different base algorithms.

5. Discussion

This study proposes a deep learning model based on the self-attention mechanism—CNN-Bi-LSTM-AM—for accurately predicting the temperature field of lithium-ion batteries across a wide temperature range. The method leverages the CNN framework to extract contextual sequence features, utilizes the Bi-LSTM framework to capture temporal dependencies, and employs a self-attention layer to enhance the similarity between input vectors.

A comprehensive performance comparison of various deep-learning networks for temperature field prediction was conducted. Training data were generated using a 3D thermal model to simulate the thermal characteristics of lithium-ion batteries under different temperature conditions. The experimental design encompasses diverse environmental conditions to evaluate the model's generalization capability and predictive accuracy. Baseline models include traditional LSTM, ARIMA, SRV, CNN, and other architectures, with performance differences assessed using RMSE and MAE metrics. Experimental results demonstrate that the CNN-Bi-LSTM-AM hybrid model, enhanced by the self-attention mechanism, outperforms other models in both accuracy and stability.

The main contributions of this study are as follows:

- The experiments show that using the CNN-Bi-LSTM-AM model for temperature field prediction achieves more satisfactory accuracy under both room temperature and low-temperature conditions;
- By incorporating CNN, the model's feature extraction capability was enhanced, enabling it to more effectively identify feature patterns under different conditions, thereby improving the model's ability to capture thermal runaway temperature field variations;
- With a slight increase in training time, our model achieves a significant improvement in accuracy while demonstrating excellent generalization capability;
- Our model is the first to address the scenario of thermal runaway heating, providing a foundation for future research on battery temperature field prediction.

Future research will focus on developing deep learning frameworks based on attention mechanisms and optimizing hyperparameter selection methods to further enhance the performance of lithium-ion battery temperature field predictions. Additionally, we plan to explore the thermal runaway characteristics of batteries, aiming to achieve precise localization of thermal runaway events based on predicted future temperatures. This research holds significant potential for industrial applications.

Author Contributions: Conceptualization, B.W.; Methodology, Z.C.; Software, Z.C.; Validation, B.W. and P.Z.; Investigation, B.W. and Z.C.; Resources, P.Z. and Y.D.; Data curation, P.Z. and Y.D.; Writing—original draft, B.W.; Writing—review & editing, B.W., P.Z. and Y.D.; Supervision, Z.C. and B.L.; Project administration, B.L. All authors have read and agreed to the published version of the manuscript.

Funding: This research was funded by the Nanchang Innovation Institute of Peking University.

Institutional Review Board Statement: Not applicable.

Informed Consent Statement: Not applicable.

Data Availability Statement: The raw data supporting the conclusions of this article will be made available by the authors on request.

Conflicts of Interest: The authors declare no conflict of interest.

References

1. Marinescu, A.; Dumbrava, I.; Vintila, A.; Marinescu, D.G.; Neagu, D.; Nicolae, V.; Radu, A. The way to engineering EV wireless charging: DACIA electron. In Proceedings of the 2017 Electric Vehicles International Conference (EV), Bucharest, Romania, 5–6 October 2017; pp. 1–6. [CrossRef]
2. Rastegarpanah, A.; Wang, Y.; Stolkin, R. Predicting the Remaining Life of Lithium-ion Batteries Using a CNN-LSTM Model. In Proceedings of the 2022 8th International Conference on Mechatronics and Robotics Engineering (ICMRE), Munich, Germany, 10–12 February 2022; pp. 73–78. [CrossRef]
3. Sun, Q.; Lv, H.; Wang, S.; Gao, S.; Wei, K. Optimized State of Charge Estimation of Lithium-Ion Battery in SMES/Battery Hybrid Energy Storage System for Electric Vehicles. *IEEE Trans. Appl. Supercond.* **2021**, *11*, 1–6. [CrossRef]
4. Hussein, S.; Abid, A.J.; Obed, A.A. ANFIS-Based New Approach for an Optimal Lithium-Ion Battery Charging Control. In Proceedings of the 2023 IEEE 3rd International Conference in Power Engineering Applications (ICPEA), Putrajaya, Malaysia, 6–7 March 2023; pp. 248–251. [CrossRef]
5. Umayal, R.M.; Darapaneni, N.; Aditya, V.; Paduri, A.R. Machine Learning based Remaining Useful Life Prediction of Lithium-ion Batteries in Electric Vehicle Battery Management System. In Proceedings of the 2023 International Conference on Communication, Security and Artificial Intelligence (ICCSAI), Greater Noida, India, 21–25 November 2023; pp. 547–551. [CrossRef]
6. Faraji, H.; Faraji, M.; El Alami, M.; Hariti, Y.; Arshad, A.; Hader, A.; Benkaddour, A. Cooling of recent microprocessors by the fusion of nano-enhanced phase change materials, Mater. *Today Proc.* **2019**, *30*, 865–869. [CrossRef]
7. Gong, X.; Xiong, R.; Mi, C.C. Study of the Characteristics of Battery Packs in Electric Vehicles with Parallel-Connected Lithium-Ion Battery Cells. *IEEE Trans. Ind. Appl.* **2015**, *51*, 1872–1879. [CrossRef]
8. Wang, H.; Yu, K.; Mao, L.; He, Q.; Wu, Q.; Li, Z. Evaluation of Lithium-Ion Battery Pack Capacity Consistency Using One-Dimensional Magnetic Field Scanning. *IEEE Trans. Instrum. Meas.* **2022**, *71*, 3507610. [CrossRef]
9. Yang, S.; Zhang, S. Energy Balance Control of Multi Group Lithium Ion Batteries Under Internet of Things Technology. *IEEE Access* **2024**, *12*, 102784–102797. [CrossRef]
10. Xu, J.; Mei, X.; Wang, X.; Fu, Y.; Zhao, Y.; Wang, J. A Relative State of Health Estimation Method Based on Wavelet Analysis for Lithium-Ion Battery Cells. *IEEE Trans. Ind. Electron.* **2021**, *68*, 6973–6981. [CrossRef]
11. Savargaonkar, M.; Oyewole, I.; Chehade, A.; Hussein, A.A. Uncorrelated Sparse Autoencoder with Long Short-Term Memory for State-of-Charge Estimations in Lithium-Ion Battery Cells. *IEEE Trans. Autom. Sci. Eng.* **2024**, *21*, 15–26. [CrossRef]
12. Naeini, A.; Cherney, E.A.; Jayaram, S.H. Temperature and electric field distributions along a form wound coil of an inverter-fed rotating machine with micro-varistor stress grading system. *IEEE Trans. Dielectr. Electr. Insul.* **2020**, *27*, 112–120. [CrossRef]
13. Duan, Y.; Chen, L.; Zhou, X.; Shi, Y.; Wu, N. Boiler Furnace Temperature Field Measurement and Reconstruction Error Elimination Based on Temperature Field Residual Correction Network. *IEEE Trans. Instrum. Meas.* **2024**, *73*, 2507215. [CrossRef]
14. Karasev, Y.V.; Pantsyrny, V.I.; Polikarpova, M.V.; Lukianov, P.A.; Gubkin, I.N.; Abdyukhanov, I.M.; Baumgartner, T.; Prokopec, R.; Eisterer, M.; Weber, H.W. Study of the Temperature and Field Dependence of the Critical Currents in Nb-Ti Strands for the ITER Poloidal Field Magnet System. *IEEE Trans. Appl. Supercond.* **2014**, *24*, 6000204. [CrossRef]

15. Kang, Y.; Ji, J.; Xu, H.; Yang, Y.; Chen, P.; Zhao, H. Swin-CDSA: The Semantic Segmentation of Remote Sensing Images Based on Cascaded Depthwise Convolution and Spatial Attention Mechanism. *IEEE Geosci. Remote Sens. Lett.* **2024**, *21*, 3003405. [CrossRef]
16. Zhang, B.; Xia, Z.; Chen, Z.; Wu, Y.; Cao, Q.; Zhou, Z.; Li, L. High Temperature Magnetization Measurement System in Pulsed Magnetic Field. *IEEE Trans. Appl. Supercond.* **2012**, *22*, 9001804. [CrossRef]
17. Kobayashi, H.; Nakada, Y.; Oike, S.; Saotome, H.; Miyagi, D.; Tsuda, M. Study on Current Behavior and Thermal Stability of No-Insulation Coils with Parallel HTS Tapes Under External Magnetic Field Fluctuation. *IEEE Trans. Appl. Supercond.* **2024**, *34*, 4903305. [CrossRef]
18. Han, X.; Cheng, Q.; Liu, F.; Yu, Y. Numerical Analysis on Thermal Tuning Efficiency and Thermal Stress of a Thermally Tunable SG-DBR Laser. *IEEE Photonics J.* **2016**, *8*, 1501512. [CrossRef]
19. Ma, Z.; Zhang, H.; Liu, J. MM-RNN: A Multimodal RNN for Precipitation Nowcasting. *IEEE Trans. Geosci. Remote Sens.* **2023**, *61*, 4101914. [CrossRef]
20. Liu, F.; Zhang, Z.; Zhou, R. Automatic modulation recognition based on CNN and GRU. *Tsinghua Sci. Technol.* **2022**, *27*, 422–431. [CrossRef]
21. Li, K.; Shen, N.; Kang, Y.; Chen, H.; Wang, Y.; He, S. Livestock Product Price Forecasting Method Based on Heterogeneous GRU Neural Network and Energy Decomposition. *IEEE Access* **2021**, *9*, 158322–158330. [CrossRef]
22. Wang, J.; Zhang, X.; Gao, G.; Lv, Y.; Li, Q.; Li, Z.; Wang, C.; Chen, G. Open Pose Mask R-CNN Network for Individual Cattle Recognition. *IEEE Access* **2023**, *11*, 113752–113768. [CrossRef]
23. Jian, W.; Li, J.P.; Akbar, M.A.; Haq, A.U.; Khan, S.; Alotaibi, R.M.; Alajlan, S.A. SA-Bi-LSTM: Self Attention with Bi-Directional LSTM-Based Intelligent Model for Accurate Fake News Detection to Ensured Information Integrity on Social Media Platforms. *IEEE Access* **2024**, *12*, 48436–48452. [CrossRef]
24. Yu, X.; Li, D. Attention Mechanism Aided Signal Detection in Backscatter Communications with Insufficient Training Data. *IEEE Trans. Veh. Technol.* **2024**, *5*, 7395–7399. [CrossRef]
25. Luo, Z.; Li, J.; Zhu, Y. A Deep Feature Fusion Network Based on Multiple Attention Mechanisms for Joint Iris-Periocular Biometric Recognition. *IEEE Signal Process. Lett.* **2021**, *28*, 1060–1064. [CrossRef]
26. Chen, Y.; Han, L.; Zhang, Y.; Zhou, Z.; Huang, P.; Li, C.; Liu, L.; Kang, J. Inner Product Accelerating Scheme Based on RRAM Array for Attention-Mechanism Neural Network. *IEEE Electron Device Lett.* **2024**, *45*, 360–363. [CrossRef]
27. Ekström, H.; Fridholm, B.; Lindbergh, G. Comparison of Lumped Diffusion Models for Voltage Prediction of a Lithium-Ion Battery Cell during Dynamic Loads. *J. Power Sources* **2018**, *402*, 296–300. [CrossRef]
28. Kim, G.-H.; Pesaran, A.; Spotnitz, R. A Three-Dimensional Thermal Abuse Model for Lithium-Ion Cells. *J. Power Sources* **2007**, *170*, 476–489. [CrossRef]
29. Coman, P.T.; Darcy, E.C.; Veje, C.T.; White, R.E. SOC Arrhenius Innernal Short Circuit. *J. Electrochem. Soc.* **2017**, *164*, A587–A593. [CrossRef]
30. Lecun, Y.; Bottou, L.; Bengio, Y.; Haffner, P. Gradient-based learning applied to document recognition. *Proc. IEEE* **1998**, *86*, 2278–2324. [CrossRef]
31. Togatorop, A.R.M.; Irawan, M.I. Nickel Price Prediction Using Bi-Directional LSTM (Bi-LSTM) and Attention Bi-Directional LSTM Network (At-Bi-LSTM). In Proceedings of the 2024 IEEE International Symposium on Consumer Technology (ISCT), Kuta, Indonesia, 13–16 August 2024; pp. 450–456. [CrossRef]
32. Dong, L.; Wang, F.; Xu, B. Self-attention Aligner: A Latency-control End-to-end Model for ASR Using Self-attention Network and Chunk-hopping. In Proceedings of the ICASSP 2019–2019 IEEE International Conference on Acoustics, Speech and Signal Processing (ICASSP), Brighton, UK, 12–17 May 2019; pp. 5656–5660. [CrossRef]
33. Zhong, R.; Wang, R.; Zou, Y.; Hong, Z.; Hu, M. Graph Attention Networks Adjusted Bi-LSTM for Video Summarization. *IEEE Signal Process. Lett.* **2021**, *28*, 663–667. [CrossRef]

Disclaimer/Publisher's Note: The statements, opinions and data contained in all publications are solely those of the individual author(s) and contributor(s) and not of MDPI and/or the editor(s). MDPI and/or the editor(s) disclaim responsibility for any injury to people or property resulting from any ideas, methods, instructions or products referred to in the content.